One-Step Fabrication of Carbon Dot-Based Nanocomposites Powering Solid-State Random Lasing

Luigi Stagi, Davide Carboni, Roberto Anedda, Radian Popescu, Yolita Eggeler, Laura Calvillo, Ashim Pramanik, Alice Sciortino, Marco Cannas, Fabrizio Messina,* and Luca Malfatti*

Carbon dots (CDs) have attracted much attention for applications in photonics and optoelectronics because of their high emission efficiency and ease of synthesis. Although studies in solution are well established, solid-state applications are less common because of optical quenching phenomena that critically affect CDs. Herein, the synthesis of amorphous CDs from citric acid, operating as hosts of dye molecules, and their incorporation into organic–inorganic silica matrices through a fast photo-induced polymerization process are reported. The photocurable sol composition allows easy dispersion of nanometer-sized scattering centers, such as titania or gold nanoparticles (NPs), which have been incorporated, along with CDs, into nanocomposites. The combination of high-brightness CDs and nanoscatterers in the hybrid matrices allows for achieving and investigating the random lasing processes occurring in the orange-red range of the visible spectrum. In situ-grown gold NPs contribute to a significant improvement in solid-state lasing, enabling an emission as narrow as 5 nm and a laser threshold as low as 0.3 mJ pulse^{-1}. The present approach reveals the technological and scientific potential of CDs when embedded in solid-state disordered active media.

1. Introduction

Carbon dots (CDs) are carbon-based nanoparticles (NPs) with remarkable optical and functional properties, offering opportunities for significant advancements in various technological fields. One of the primary advantages of CDs is their simple synthesis that often utilizes low-cost precursors and eco-friendly treatments and allows producing NPs with high quantum yield (QY),[1,2] biocompatibility,[3] and customized chemical functionalities on the surface.[4,5] Notably, CDs exhibit strong fluorescence across the UV,[6] visible,[7] and infrared ranges,[8,9] depending on their structure. This structure is heavily influenced by the synthesis methods and the selection of precursors, which affect the presence of aromatic groups, conjugated bonds, and heteroatoms.[10,11] Despite the difficulty in categorizing the various types of CDs, it is currently recognized that they can be described as graphene quantum dots (GQDs) if they resemble small fragments of graphene, carbon quantum dots (CQDs),[12,13] or carbon nanodots (CNDs) if they are characterized by a mixed structure comprising both a crystalline (graphitic) and an amorphous part.[14] Finally, carbonized polymer dots (CPDs) are determined by a predominantly polymeric structure.[15] Citric acid (CA) is probably the most relevant coprecursor involved in the common syntheses of CDs, which are hydrothermal, solvothermal methods, and precursors pyrolysis. CA is a cheap and generally biocompatible reagent that further helps reducing the production cost of some specific CDs syntheses characterized

L. Stagi, D. Carboni, L. Malfatti
Laboratory of Materials Science and Nanotechnology (LMNT)
CR-INSTM
Department of Biomedical Sciences
University of Sassari
Viale S. Pietro 43/B, 07100 Sassari, Italy
E-mail: luca.malfatti@uniss.it

R. Anedda
Porto Conte Ricerche s.r.l., Strada Provinciale S.P. 55
Loc. Tramariglio, 07041 Alghero, Italy

ⓘ The ORCID identification number(s) for the author(s) of this article can be found under https://doi.org/10.1002/sstr.202400498.

R. Popescu, Y. Eggeler
Laboratory for Electron Microscopy (LEM)
Karlsruhe Institute of Technology
Engesser str. 7, 76131 Karlsruhe, Germany

L. Calvillo
Department of Chemical Sciences
University of Padua
Via Marzolo 1, 35131 Padua, Italy

A. Pramanik, A. Sciortino, M. Cannas, F. Messina
Department of Physics and Chemistry "Emilio Segrè"
University of Palermo
Via Archirafi 36, 90123 Palermo, Italy
E-mail: fabrizio.messina@unipa.it

**ADVANCED
SCIENCE NEWS**

www.advancedsciencenews.com

**small
structures**

www.small-structures.com

by low yields due to the purification process.[16,17] Additionally, CA generally promotes the biocompatibility and the stability of the molecules incorporated into the CD matrix.[18] The low melting point of CA facilitates the growth of a carbon framework around emission centers, enhancing the resistance of the emissive centers to photobleaching and concentration quenching. For these reasons, CA-based CDs appear to have potential for solid-state applications.[19]

To design innovative optical nanosystems, it is essential to precisely engineer the photophysical properties of CDs to achieve a system with strong and narrow emissive performance.[20] This is particularly important for CDs with abundant aromatic groups and sp^2 domains, such as GQDs and CNDs, where solid-state self-quenching is a main concern. In contrast, CPDs and amorphous CDs tend to remain fluorescent as powders, because they minimize the mutual interactions between the emitting centers, including both molecular fluorophores and functional groups.[21] In most of the syntheses, the emission properties of CDs are due to small molecular chromophores spontaneously formed during the carbonization reactions along with the carbonaceous core. While the spontaneous formation of fluorescent molecules is of extreme interest for the low-cost development of luminescent NPs, the poor control of the carbonization reactions severely limits the ability to precisely control the optical response of CDs.

An alternative approach involves embedding deliberately molecular fluorophores of known optical properties into the carbonaceous matrix, by introducing them as reactants in the synthesis from the very beginning. In a recent work,[22] we have demonstrated the benefits of embedding specific molecules within an amorphous carbonaceous matrix, highlighting the superiority of the CD-fluorophore system, as compared to the bare fluorophore in itself, in terms of resistance to photobleaching. In particular, we have utilized safranin O (SO), a molecule widely used in histology and cytology as a biological stain, to make a CD featuring high SO concentrations and photobleaching-resistant properties. Despite the poor quantum efficiency of SO (<6%) that prevents the photonic applications of bare SO, especially at solid-state, the work proved the protective effect of the carbonaceous matrix offering promising results in photonics and optoelectronics.

Using CDs in solid-state applications poses challenges, such as low quantum efficiency and the need for a transparent, inert matrix to prevent quenching of the optical emitter. Incorporating CDs in a solid-state matrix may also decrease the matrix optical quality by promoting Rayleigh scattering. Furthermore, depending on the solvent solubility of CDs, one can observe a phase separation during the matrix synthesis, making inhomogeneous solids. Mechanisms such as low solubility or inadequate dispersion represent some of the main problems in solid-state device preparations. The sol–gel technique is a promising strategy for this purpose, enabling the creation of transparent silica-based matrices with substantial organic content. These organic–inorganic hybrid matrices can incorporate large amounts of active compounds and form monoliths of sufficient thickness for photonic applications, where structural and thermal stability, as well as high efficiency, are crucial. One such application is fabricating narrowband and bright solid-state light emitters based on amplified stimulated emission and random lasing phenomena.[23,24] While many studies have explored CDs as optical media for laser applications, most of them have focused on CDs in solution within an optical cavity as feedback. Fewer studies have examined CDs exhibiting random lasing characteristics, where lasing feedback is provided by scattering centers that amplify partially localized light.[25,26] Even rarer are studies of solid-state CDs in which both the optical medium and scattering centers are fixed in place within a single, self-standing solid system.

In this work, we report on the study of CDs, loaded with Rhodamine B (RhB), for solid-state optical applications. The CDs were fabricated through CA pyrolysis, which provided a versatile framework to accommodate RhB molecules at different concentrations, preventing their aggregation-induced solid-state quenching. CDs were initially dispersed in a photocurable silica-based organic–inorganic solution that was subsequently converted to a solid-state matrix by UV photopolymerization. The resulting monoliths display random laser emission, with performance-enhancing as the concentration of RhB doping increases. Optimization of the random lasing phenomenon was also studied by introducing external scattering centers, such as gold NPs, which were in situ grown during photocuring. This approach allowed us to develop a one-step UV-photo-assisted synthesis of solid-state nanocomposites characterized by random laser emission.

2. Methodology

2.1. Materials

CA anhydrous (purity >99%) (Alfa Aesar), 3-(Trimethoxy silyl) propyl methacrylate (TMSPMA, 98%) (Sigma), tetraethylorthosilicate (TEOS) (Aldrich, 99% purity), ethyl-2,4,6-trimethylbenzoylphenyl-phosphinate (TBP) (BASF, commercially available as Lucirin TPO-L), ethanol (EtOH) (ACS Reagent, >99.5%), hydrochloric acid (HCl) (Sigma-Aldrich, 1 N), Rhodamine B (RhB), (Sigma-Aldrich, Milano, Italy, CAS 81-88-9), Titanium (IV) oxide (TiO$_2$ NPs, 20 nm particle size) (Aldrich), gold (III) chloride trihydrate (HAuCl$_4$) (Merck, purity > 99.9 %), and deionized water were used without further purification.

2.2. Synthesis

2.2.1. CDs Preparation

CA crystalline powders (3.84 g, 0.02 mol) were placed into a 50 mL round flask and heated up to the melting point, ≈160 °C, in an oil bath. After melting, a Teflon-coated stirring bar was activated at a stirring rate of 200 rpm and RhB powders were added to the melted CA. After RhB was completely dissolved, the temperature was raised to 180 °C and the reaction was allowed to take place at the target temperature for 1 h. The reaction was then quenched in air and the dark gel was collected by ethanol and dried at 60 °C for 24 h. The powder was then purified in distilled water through dialysis bags (cut off ≈2 000 Da) for 24 h, replacing water every hour in the first 6 h. The dialysis process was evaluated by monitoring the UV–vis spectrum of the dialysis solution. The release of rhodamine and other byproducts was tracked using UV–vis

**ADVANCED
SCIENCE NEWS**

www.advancedsciencenews.com

**small
structures**

www.small-structures.com

spectroscopy until their presence became negligible in the dialysis solution. Water was then evaporated at 60 °C for 48 h.

CDs with different amounts of RhB were synthesized by adding 5, 10, and 50 mg of RhB to 3.84 g of melted CA. The samples were named CAR5, CAR10, and CAR50. Undoped CDs were named CA180. CAR10 samples were also collected at three different reaction times for analysis: CARt0 (0 min), CARt15 (15 min), CARt30 (30 min), and CARt45 (45 min) for nuclear magnetic resonance (NMR) investigations.

2.2.2. Silica Monoliths and Films Fabrication

Organic–inorganic silica hybrids were obtained by photopolymerization of a silane-based sol. 0.75 mL of TEOS was mixed with 1.76 mL of TMSPMA. After vigorously stirring for 1 min, 100 μL of EtOH and 100 μL of HCl (1 N) were added to the solution and kept under stirring for another 1 min. 60 mg of CARs were dissolved in the sol for the CD-doped matrix. The molar ratios were TEOS:TMSPMA:EtOH:HCl(1 N) = 1:2.05:1.97:0.03. 100 mg of a photoinitiator (TBP) was added to the solution under stirring at 200 rpm. The obtained solution was poured into a mold or deposited by spin-coating at 1500 rpm for 30 s. The deposited materials were cured with UV irradiation by using a LED Zolix MLED4-2 UV-LED at 365 nm with a power of 100 mW cm^{-2} for 5 min.

Scattering NPs were introduced in the matrix using titania NPs (TiO$_2$ NPs) and in situ growth gold NPs (Au NPs). The former were dispersed in the sol before adding TBP. The latter were grown directly during the photopolymerization process by adding 100 μL of an ethanolic solution HAuCl$_4$ at three different concentrations (10, 30, and 60 mg mL^{-1}). Also in these cases, the UV exposure time was kept at 5 min.

2.3. Characterization

Thermogravimetry-differential scanning calorimetry (TGA-DSC) analysis was performed using an SDTQ600 (TA instruments). All thermogravimetric analyses were done under a nitrogen (N$_2$) atmosphere.

Samples were deposited on a silicon substrate to perform X-ray diffraction (XRD) measurements. XRD patterns were acquired using a Bruker D8 Discover diffractometer under irradiation with a Cu Kα$_1$ line (=1.54056 Å); the X-ray generator worked at a voltage of 40 kV and a current of 40 mA.

Absorption Fourier-transform infrared (FTIR) spectra were recorded by a Vertex 70 interferometer (Bruker) in the 4000−400 cm^{-1} range with a 4 cm^{-1} resolution and 32 scans. The spectra were recorded using KBr pellets with 1 mg of sample and 500 mg of KBr. Samples were also recorded in attenuated total reflection (ATR) mode.

The NMR spectra were acquired on a Bruker Avance 600 spectrometer (Bruker Biospin, Karlsruhe, Germany) operating at the Larmor frequency of 600.13 MHz for protons and 150.90 MHz for ^{13}C, equipped with a 5-mm BBI probe, in deuterated dimethyl sulfoxide (99.8%, Cambridge Isotope Laboratories Inc., Andover, MA, USA). 1D proton spectra were acquired with a pulse of 10.95 μs and 64 scans. The pulse was optimized to 90° (12.6 μs) for acquiring 2D maps. Gradient-selected ^{1}H-^{13}C heteronuclear single quantum coherence (HSQC) and heteronuclear

multiple bond correlation (HMBC) experiments were acquired with 256 increments, each containing 2048 or 4096 data points, respectively. For acquiring the HSQC, 128 scans and 4 dummy scans were accumulated, with J(^{13}C-^{1}H) = 145 Hz and a spectral window of 7 k × 33 201 Hz. 16 scans and 16 dummy scans were acquired with an HMBC sequence optimized for long-range couplings (J = 10 and 145 Hz) and with suppression of one-bond correlations, over a 9 k × 33 518 Hz spectral width. 2D homonuclear shift correlation was performed using a COSY sequence with gradient pulses, acquiring 128 spectra of 2048 data points, 16 scans and 16 dummy scans, and spectral windows of 6 k × 6 k Hz. All NMR experiments were carried out at 298 K (Bruker BVT3000 and BCU05 units, Bruker Biospin, Karlsruhe, Germany) and using a relaxation delay of 3 s for 1D and 2 s for 2D experiments.

UV–vis spectra were measured in absorbance mode from 200 to 600 nm by using a Nicolet Evolution.

300 UV−vis spectrophotometer (Thermo Fisher). A concentration of 0.8 mg mL^{-1} CDs dispersed in water was used for the analysis.

Fluorescence analysis of the samples solubilized in water was done using a Horiba Jobin Yvon NanoLog spectrofluorometer with an excitation and emission wavelength ranging from 300 to 700 nm. A concentration of 0.1 mg mL^{-1} was used for the analysis.

Time-resolved photoluminescence (PL) was performed using the TBX picosecond detection module connected to the spectrometer and the samples were excited with a LED at 340 nm (1 MHz repetition rate and pulse width <1.2 ns).

Absolute QY (PLQY) was measured by an integrating sphere (Labsphere 3PGPS053SL) internally covered by Spectralon. The PLQY was calculated via the following formula: PLQY = I_s/$(S_r - S_s)$, where I_s refers to the spectrally integrated PL of the sample. S_r and S_s are the spectrally integrated scattering signal around the excitation wavelength of respectively the reference (bare SiO$_2$ matrix) and the sample, i.e., RhB or CAR10 hosted inside SiO$_2$ matrix.

The thickness and refractive index of films deposited on quartz substrates were measured using an Alpha-Spectroscopic Ellipsometer (α-SE^{TM}) from J.A. Woollam, USA. The measurements were analyzed with a Cauchy film model.

The transmission electron microscopy (TEM) samples were prepared at room temperature in the air by drop-casting a diluted suspension of NPs dispersed in ethanol onto a commercial TEM SiO$_2$ grid (thickness of 20 nm) (SIMPore).

The CD composition was determined by X-ray photoelectron spectroscopy (XPS) using a custom-designed UHV system equipped with an Omicron electron analyzer, working at a base pressure of 10^{-10} mbar. A non-monochromatized Al Kα X-ray source (1476.6 eV) was used to acquire the core-level photoemission spectra. Single spectral regions were collected using 0.1 eV steps, 0.5 s collection time, and 20 eV pass energy.

The size and the chemical composition of CDs and Au NPs on the SiO$_2$ substrate were investigated by high-angle annular dark-field (HAADF) scanning transmission electron microscopy (STEM) in combination with energy-dispersive X-ray spectroscopy (EDXS) carried out on a FEI Osiris ChemiSTEM microscope at 200 keV electron energy, which is equipped with a Super-X EDXS system comprising four silicon drift detectors.

**ADVANCED
SCIENCE NEWS**

www.advancedsciencenews.com

**small
structures**

www.small-structures.com

EDXS spectra obtained during scanning of a rectangular area, including inside a single CD, were used to determine its chemical composition (EDXS area scans). The identification of CDs on the substrate was performed by using the C-K$_\alpha$ line. The EDXS line of C (C-K$_\alpha$ line) from CDs, X-ray characteristic lines of the Si-K series, and the O-K$_\alpha$ line from the TEM grid, as well as of the Cu-K and Cu-L series from the Cu clamp were observed on all EDXS spectra. Alternatively, EDXS elemental maps of C (C-K$_\alpha$ line), Si (Si-K$_\alpha$ line), and O (O-K$_\alpha$ line) were recorded and used to prove the formation of CDs on the SiO$_2$ substrates. The maps were analyzed by using the ESPRIT software (version 2.3) from Bruker. Histogram of size distribution was calculated for 1100 C dots recorded on many HAADF-STEM images with different magnifications.

Atomic force microscopy (AFM) was performed with a microscope NT-MDT Ntegra at 0.2 Hz scan speed in semicontact mode, using a silicon tip with a typical resonance frequency of 240 kHz, 11.8 Nm^{-1} force constant and 10 nm typical curvature radius.

For random lasing experiment, a tunable pulsed laser system (5 ns, 10 Hz, OPOTEK VIBRANT) was used as the pump source. The pump beam of wavelength 540 nm was first passed through an aperture of diameter 6 mm, and then focused to the sample position by use of a plano-convex cylindrical lens ($f = 5$ mm). The SiO$_2$ monoliths, loaded with gain media (red emitting CDs), semiconductor and plasmonic scatterers, were then positioned slightly away from the focal point of the lens and pumped with variable intensities. The cylindrical lens was mounted on a micrometric translation stage to optimize the excitation spot size on the sample for better results. In the best experimental conditions, the estimated vertical width of the excitation line on the surface of the sample was about 150 μm. The emission from the excited sample was collected by an optical fiber (AVANTES, 200 mm core, numerical aperture 0.22) positioned ≈5 cm away from the sample cuvette. The optical fiber was finally connected to a spectrometer (Avantes, Star Line ULS2048CLEVO, resolution 1.4 nm) for spectral analysis of the emitted light. Each emission spectrum, shown in this work, is extracted by averaging at least 500 pump shots. The same laser source was also utilized to investigate the time-resolved PL profile under excitation at 532 nm, by collecting spectra at several delays from the laser pulse on an intensified charge-coupled device camera.

3. Results and Discussion

3.1. Structural Properties

CA/Rhodamine B-based CDs (CARs) were obtained through a pyrolysis process of CA. Increasing amounts of RhB (5,10, 50 mg for CAR5, CAR10, and CAR50, respectively) were dissolved in molten CA at a temperature of 160 °C to allow homogeneous mixing. The solution was then raised to a temperature of 180 °C and allowed to react for 1 h. RhB has the advantage of being a stable dye throughout the temperature range adopted for CDs formation.[27] The various steps of the synthesis, depicted in **Figure 1**a, were chosen by monitoring the TGA and DSC curves of the CA-RhB system up to a temperature of 300 °C. The treatment produces quenching-resistant powder under UV irradiation as shown in Figure 1b. CARs dispersed in ethanol appear as a red solution, in marked contrast with RhB dye which appears of pink color when dissolved in the same solvent (Figure 1c). In DSC curve is characterized by a first endothermic event at ≈156 °C with no significant weight loss that corresponds to CA melting (Figure 1d). The melting is completed at 171 °C but is accompanied with a sequence of minor events, at least two, terminating at 232 °C. These are characterized by an overall weight loss of almost 83% and indicate the decomposition of CA. It is known that after the melting step, CA undergoes dehydration and decarboxylation processes that lead to the formation of various intermediates. Initial dehydration results in the formation of aconitic acid, which is usually not stable and tends to form itaconic acid (**Scheme 1**) and finally maleic (citraconic) anhydride.[28,29] The recorded events are associated with the decomposition of intermediate compounds that formed right after the dehydration process. The thermal decomposition products of CA form the basis for the formation of cyclic structures and, in the presence of coreagents, polymeric structures.[30,31]

In connection with the thermal analysis of the CA-RhB as a function of the temperature, the CDs formation was isothermally
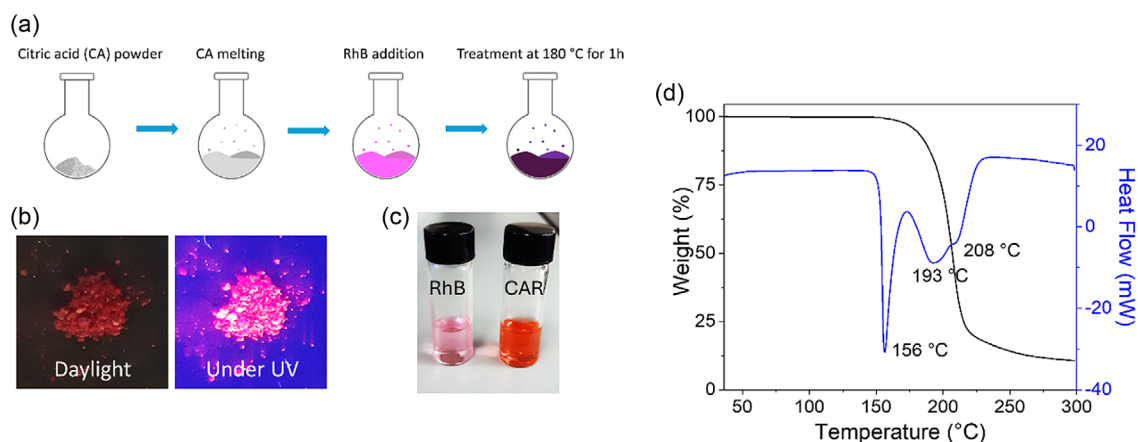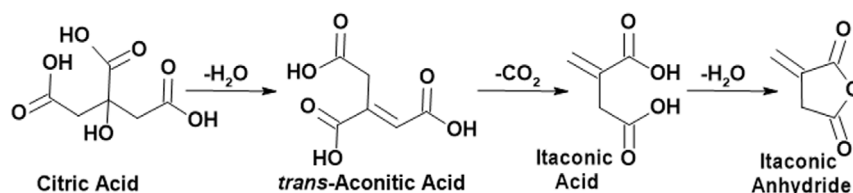

Figure 1. a) Scheme of the CARs synthesis method. b) Optical appearance under daylight and solid-state emission ($\lambda_{ex} = 365$ nm) of CARs powders. c) Images of ethanolic solutions of RhB and CARs. d) DSC-TGA analysis of CA and RhB combined in 1:0.04 molar ratio.

**ADVANCED
SCIENCE NEWS**
www.advancedsciencenews.com

**small
structures**
www.small-structures.com

Scheme 1. Transformation of CA into itaconic anhydride.

monitored at the temperature of 180 °C, as the product formation processes also occur at this temperature. The isothermal DSC curve is reported in Figure S1 (Supporting Information). In this analysis, the CA was brought to $T = 180$ °C with a ramp of 10 °C min^{-1} and maintained at a constant T for 1 h. In the first 30 min, the three main events of melting and decomposition of CA are observed. At the same time, weight loss of around 60% is measured. This indicates that the creation of CDs involves a complex dehydration and condensation process, which deserves to be investigated by different analyses.[15]

FTIR and NMR measurements were carried out to address the structure of CARs (**Figure 2** and **3**). At high wavenumbers, CA is characterized by four distinct bands at 3495, 3296, 3450, and 3222 cm^{-1}, attributed to OH stretching of carboxyl groups.[22] Anhydrous CA exhibits two characteristic bands at 1744 and 1692 cm^{-1} corresponding to C=O stretching of the carboxyl groups, free and hydrogen bonded respectively.[32] Multiple narrow vibrational modes are also observed in the regions between 1468–1269 cm^{-1} and 1269–1000 cm^{-1}. The first range is mainly due to CH$_2$ (scissoring and rocking vibrations)[33,34] while the second is due to C—O—H and C—O stretching.[35] The spectrum of RhB is characterized by narrow molecular vibrations originating from the xanthene structure and its dimethylamino groups. C—H stretching vibrations of phenols and aliphatic groups determine the pattern at high wavenumbers (>2800 cm^{-1}) along with OH stretching of carboxyl groups. We attribute the mode at 1688 and 1580 cm^{-1} to the stretching of the carboxyl C=O.[36]

Several additional modes appear in the region at intermediate wavenumbers, resulting from the stretching and bending of C=C, C—C, and C—H bonds in the structure's aromatic systems.

Infrared spectra of CDs are reported in Figure 2 for three different RhB concentrations (CAR).

The infrared spectra of CAR5, CAR10, and CAR50 are similar as they appear largely dominated by absorption bands attributed to the carbonaceous matrix of the CDs. The matrix forms as a result of the dehydration and decarboxylation processes of CA at elevated temperatures. After heat treatment, along with dehydration and decarboxylation processes, the structure of CA transforms into a disordered carbonaceous structure, characterized by a prominent C=O stretching feature between 1700 and 1703 cm^{-1}. This feature is very commonly observed in CA-derived CDs and is present in both amorphous[22] and graphitic CDs.[34] Similarly, the regions of CH$_2$ bending and C—O stretching turn in two broad bands around 1403 and 1176 cm^{-1} as a result of a disordered structure retaining a variety of C—H and oxidized carbon. The high concentration of alkene C—H is also evidenced by the bands at 2974 and 2937 cm^{-1}. The spectrum properties of the various CARs can be found in CDs produced from CA alone, as shown in Figure S2 (Supporting Information), demonstrating that the final structure of CARs is mainly due to the transformation of CA into an amorphous carbonaceous structure. However, the presence of RhB in CAR affects the vibrational spectra of CDs as evidenced by the emergence of a new vibrational mode around 1763 cm^{-1}, whose intensity increases with the dye concentration (Figure 2b). This vibration is also attributed to an ester bond formed due to a high-temperature reaction between carboxyl groups.[37] Although these COOH groups could involve the carbonaceous matrix and RhB, it is unlikely to detect RhB contribution due to its low molar concentration. In fact, treating CA180 at a higher
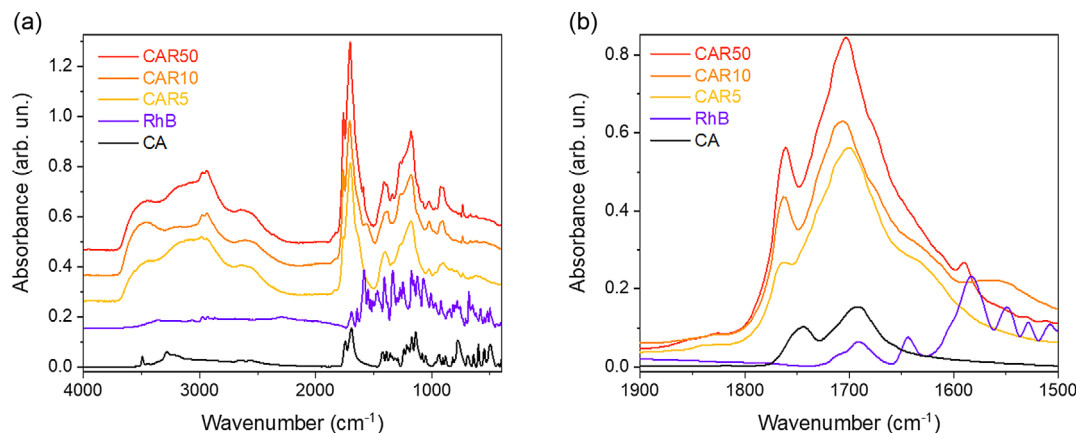

Figure 2. a) FTIR absorption spectra of CARs with different concentrations of RhB and CA and RhB precursors. b) Ester bond formation: FTIR spectra in the range between 1900 and 1500 cm^{-1}.
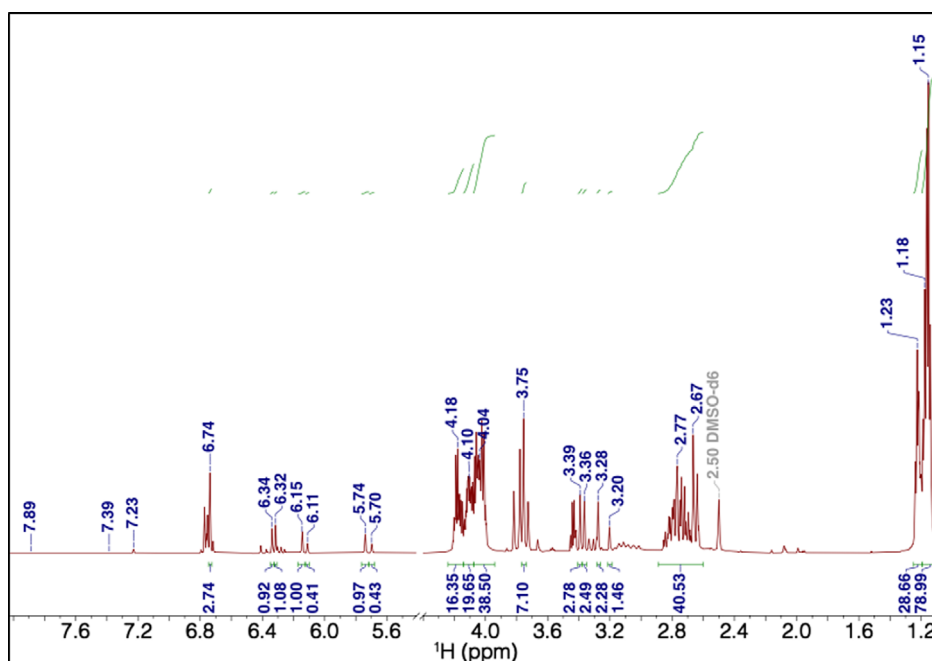
**ADVANCED
SCIENCE NEWS**

www.advancedsciencenews.com

**small
structures**

www.small-structures.com

Figure 3. 1D-NMR of CA in d6-DMSO treated at 180 °C for 1 h.

temperature results in a similar band formation, which appears slightly shifted at 1772 cm^{-1} (Figure S3, Supporting Information). RhB influences the matrix formation process. As RhB concentration increases, it appears to promote the formation of ester groups between carboxyl groups in the carbonaceous NPs.

To understand how the presence of RhB could affect the thermal degradation of CA, 1D-NMR and 2D-NMR (TOCSY, HSQC, and HMBC) (Figure S4–S6, Supporting Information) studies of the thermal degradation of CA were performed in the absence of Rhodamine B. The analysis of 1D-NMR of CA (Figure 3) highlights the presence of starting material (a pair of multiplets, **δ** 2.67 and 2.77 ppm, corresponding to the methylene groups of CA) and different species derived from its thermal decomposition according to Scheme 1.

The dehydration of the CA leads to two isomers of aconitic acid. The major product is the *trans*-aconitic, whose presence is confirmed by the correlation of the signals from its olefinic protons (**δ** 6.74 ppm) with those of the methylene group at **δ** 3.75 ppm in the total correlation spectroscopy (TOCSY) (Figure S4, Supporting Information). The dehydration leads also to *cis*-aconitic isomers, which are evidenced by two pair of olefinic signals (**δ** 6.34 and 6.32 ppm) coupled with the corresponding methylene groups (**δ** 3.36 and 3.39 ppm). The aconitic acid undergoes a decarboxylation leading to two slightly different itaconic structures characterized by two terns of signals (**δ** 6.15, 5.74 and 3.28 ppm) and (**δ** 6.11, 5.70 and 3.20 ppm) with the two downfield shifted signals corresponding to the olefinic protons. Another couple of signals, **δ** 7.39 and 7.89 ppm, clearly correlated in the TOCSY map, are reasonably strongly downfielded signals of olefinic protons derived from a polymerization pattern that left the alkene structure intact. Interestingly, the NMR spectra suggest that most of the mass sample is not given from the species

described above but rather from species characterized by three different methyl groups (**δ** 1.15, 1.18, and 1.23 ppm) which couple with corresponding methoxy groups, —CH$_2$O— (**δ** 4.04, 4.10, and 4.18 ppm), as evidenced by the TOCSY correlation. These signals could be likely related to the backbone structure of the CDs.

To understand how the presence of 10% mol of RhB could affect the formation of CARhB-CDs, we have monitored the reaction kinetic of the CD formation at 180 °C every 15 min up to 45 min (**Figure 4**). The full 1D-NMR spectrum of Rhodamine B in d$_6$-DMSO (Figure S7, Supporting Information) was acquired to allow an easier identification of the RhB signal in the spectra of the CA prepared with 10% mol of RhB. At $t = 0$ min, the 1D-NMR shows the presence of CA, evidenced by the multiplet centered at 2.65 ppm, and a very low signal ascribable to the olefinic proton of the *trans*-aconitic acid (*vide supra*). From the signals integration it appears that the ratio citric:aconitic is about 29:1 while all the other species are irrelevant. Moreover, two groups of signals around 1.2 and 4.1 ppm, which correlate in a 3:2 ratio, respectively, induce to hypothesize a —CH$_3$ group coupled with a —CH$_2$O— moiety, though the origin of these signals in unclear.

At $t = 15$ min, the signals of CA decrease and *trans*-aconitic acid increase together with the new signals of the itaconic derivatives, obtained from the decarboxylation of the *trans*-aconitic. The integration of signals evidences a 2:1 ratio of the itaconic derivatives with respect to the aconitic acid whilst there is still a large presence of CA highlighted by a 11:3 ratio when compared to the new species. Interestingly, a new spin system, present only in the sample containing RhB, appears at around **δ** 2.0 ppm with three distinct signals (**δ** 1.96, 1.99, and 2.07 ppm). It is reasonable to assign these signals to methyl groups of citraconic derivatives, obtained from the isomerization of the itaconic structure. This assumption is further corroborated
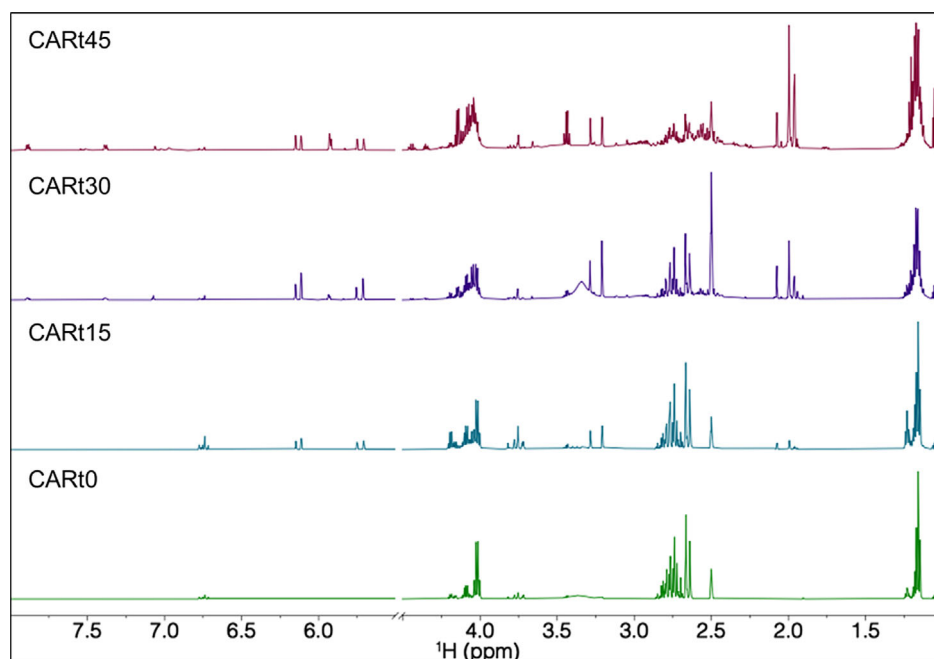
Figure 4. From bottom to top: 1D-NMR of CARhB-180 in d6-DMSO acquired after 0 (CARt0), 15 (CARt15), 30 (CARt30), and 45 min (CARt45) from the addition of RhB to the melted CA.

by the rising multiplet around 5.9 ppm, which is attributed to the olefinic protons of the citraconic derivatives.

The spectrum profile after 30 min of reaction is enriched with new downfield low-intensity signals (i.e., δ 7.39 and 7.89 ppm). Interestingly, the *trans*-aconitic acid is no longer the most abundant product of the degradation since it is replaced, in this role, by the itaconic and especially citraconic derivatives. It is noteworthy that some aromatic signals related to the presence of RhB (δ 6.97, 7.07, 7.49, and 8.22 ppm) become more evident.

After 45 min of reaction, the signals of the olefinic protons related to the degradation products are almost negligible with respect to the signals of the aliphatic region, particularly that around 2.0 ppm, which is instead consistent. The original signals of the CA have changed and shifted (2.57 ppm) and they could be therefore attributed to the CD backbone, together with the shifted signals around 4.00 and 1.16 ppm.

The differences between the two reaction mixtures, with and without RhB after 1 h at 180 °C, are highlighted in Figure S8 (Supporting Information) by comparing the corresponding spectra. The citraconic derivatives are, in fact, almost negligible in the absence of RhB while they assume a clear relevance in its presence. From an evaluation of the integrals of the olefinic protons,

it is possible to estimate approximately a 1:1 ratio of the citraconic:itaconic species. This difference can be explained by considering that the tertiary nitrogen of RhB plays a crucial role in catalyzing the isomerization of itaconic anhydride into citraconic anhydride, increasing its reaction rate thanks also to the thermal treatment.[38,39] The citraconic anhydride can undergo subsequent hydrolysis leading to the citraconic and mesaconic acids. The reaction sequence is reported in **Scheme 2**.

The large number of degradation products of CA produced by the thermal treatment does not allow a clear assignment of all the peaks. However, NMR allows to follow the transformation of the original CA into some of the degradation products and a tentative attribution is proposed for the backbone signals. As hypothesized by Cody et al.[40] during the degradation of CA a large number of derivatives can be formed. Among the possible occurring reactions, one is worth of mention for being accountable for a possible polymerization pathway leading to the CDs backbone: the condensation of a carboxylic acid with an olefin to give an ester. Moreover, the concentration of RhB incorporated into the CD is minimal compared to the overall carbonaceous structure. As a result, its signals are overshadowed, making it challenging to distinguish them from those associated with the ester linkage in the
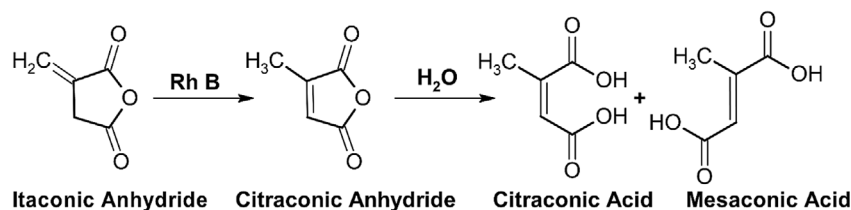
Scheme 2. Transformation of itaconic anhydride into citraconic anhydride and its hydrolysis in citraconic and mesaconic acids.

ADVANCED
SCIENCE NEWS

www.advancedsciencenews.com

small
structures

www.small-structures.com

pyrocitric backbone. It is however reasonable to infer that RhB was integrated into the matrix via an ester linkage formed by its free carboxylic group.

Figure S9a (Supporting Information) shows the C 1s XPS region of CA reference, which can be separated into three components at 284.8, 286.3, and 288.7 eV, attributed to C—C, C—OH, and COOH species. After the treatment at 180 °C, new components are observed which can be explained by the decomposition and polymerization processes of the CA molecules. The CA180 sample shows five components at 284.4, 285.4, 286.3, 288.0, and 288.7 eV attributed to sp^2, and sp^3 carbon, —OH/C—O—C, carbonyl, and carboxylic/ester groups, respectively. The presence of the C sp^2 component confirms the formation of a carbonaceous structure made of sp^2 and sp^3 carbon due to the polymerization of the CA molecules that constitute the CDs backbone, in agreement with the FTIR and NMR results. In contrast, the decrease of the carboxylic species and the formation of carbonyl groups is in agreement with the formation of a variety of derivative products, like aconitic and itaconic acids, due to the decomposition/polymerization processes of the CA molecules.

CAR10 exhibits the same components as CA180 but with a different ratio. An increase in the C sp^2 and C sp^3 components is observed due to the addition of rhodamine. The decrease of the C—OH component can be related to the formation of an ester bond between the CA and RhB. However, the formation of this bond cannot be confirmed by XPS since it overlaps with the component assigned to carboxylic groups. The XPS analysis is reported in Table S1 (Supporting Information).

Figure S9b (Supporting Information) reports the N 1s region of the CAR10 sample. The high noise/signal ratio is due to the small amount of RhB compared to the carbon matrix. The spectrum can be deconvoluted into two components at 399.4 and 401.9 eV related to $N-(C)_3$ and $C{=}N^+{-}(C)_2$, respectively. The two expected components confirm that RhB does not decompose during the thermal treatment at 180 °C.

The morphology and structure of the CARs are shown in **Figure 5**a,b. HAADF-STEM measurements, specifically carried out on the CAR10 sample, show the presence of carbonaceous particles with an average size of 37 nm (Figure 5b). High-resolution TEM (HRTEM) images, shown in Figure S10 (Supporting Information), show the formation of amorphous C dots as indicated by the absence of any structural details (lattice fringes) within particles. Moreover, the absence of an ordered structure, whether graphenic or graphitic, is also supported by X-ray measurements, shown in Figure S11 (Supporting Information).

The diffraction pattern consists of a single, very broad band centered at ≈20°, typically attributed to an amorphous structure.[41] EDXS elemental maps performed on the silicon substrate clearly show the carbonaceous nature of the particles and the absence of heterogeneous elements in the structure (Figure S12, Supporting Information).

The measurements obtained by AFM are in agreement with those reported for TEM. The investigation of the image profile (Figure 5c,d) shows a particle distribution ranging from 10 to 30 nm. The particle height distribution was also calculated by
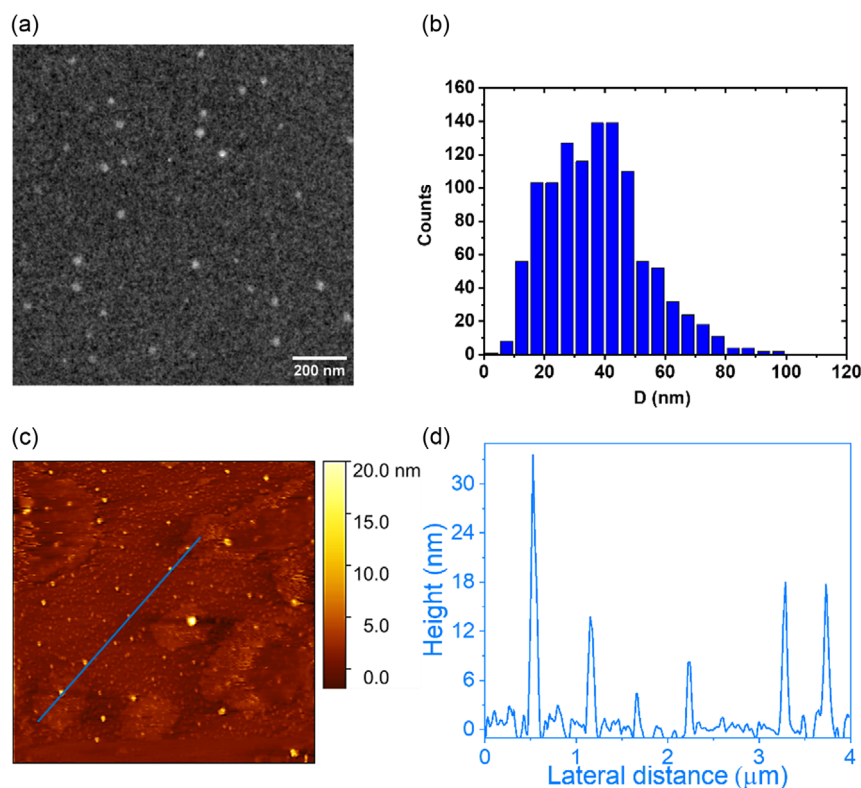

Figure 5. a) HAADF-STEM image of CAR10. b) Histogram of size distribution calculated by TEM images. c) AFM image of CARs on Si substrate. d) Corresponding height profile along the blue line in (c).

averaging the size of 138 NPs retrieved on a $30 \times 30\,\mu m$ sample area, achieving a value of around 25.5 nm (Figure S13, Supporting Information), slightly below that observed for TEM.

3.2. Photophysical Properties

Figure 6a shows the UV–vis spectrum of four CDs samples obtained at varying RhB concentrations. Absorption of CA180 is predominant in the UV region, with a tail extending slightly beyond 400 nm. Absorbance shows the greatest contribution below 300 nm, a region attributable to the π–π* transition of the C=C bonds.[5,42] It is therefore compatible with the presence of sp^2/sp^3 carbon matrix as a result of CA condensation. At about 333 nm a broadband emerges for the n–π* transition due to the presence of the C=O bonds. These spectral features are compatible with the previously reported GQDs from pure CA, although the n–π* band appeared redshifted by 20 nm,[43] demonstrating the influence of the carbonaceous backbone on the general characteristics of the CD. The addition of RhB does not significantly perturb the UV–vis spectrum of the carbon matrix. CAR5 and CAR10 show a sharper absorption band at 330 nm, which is probably the result of conjugation with RhB, whose carboxylic group reacted to form an ester bond, and the RhB characteristic absorption which falls at 550 nm.

Higher RhB loadings markedly modify the photophysical response of CDs, as can be observed in the CAR50 sample. Indeed, the CAR50 spectrum reveals not only the obvious increase in RhB absorption at 550 nm, but also a general enhancement of the UV absorption of the NPs, with the appearance of two distinct local maxima at 333 and 357 nm attributed to the C=O in the CD structures and RhB, respectively. Given the highly disordered structure, we suppose that the increase in RhB during the synthesis phase influences the formation of the higher-energy C=C carbon bonds with its aromatic structure, and consequently a total increase across the spectrum in the UV.

The comparison between the UV absorption and the excitation spectra measured at the PL maximum of 572 nm is reported in Figure 6b. The excitation spectrum closely matches the characteristic absorption profile of the RhB dye (Figure 6a). The lack of influence of the matrix on the incorporated dye indicates that the carbon framework serves as an inert host. This suggests that the RhB molecules experience minimal influence from the external chemical environment. In contrast, the absorption spectrum significantly deviates from the excitation spectrum, with several additional absorption components in the deep-UV that do not contribute to the emission. This implies that absorption from the carbonaceous matrix does not result into an energy transfer to the emissive dye. **Figure 7**a shows the two-dimensional excitation-emission fluorescence intensity map of CAR10 in powder state. Besides a weak contribution of the blue-emitting carbon framework, the emission at the solid state is governed by the embedded RhB molecules. Differently from CAR in solutions, the PL maximum is redshifted to 590 nm and exhibits a wide excitation range from 350 nm up to 565 nm. When incorporated into the CDs, the RhB dye emission becomes quenching-resistant, as exhibited by Figure 7b. On the contrary, dried RhB powders are almost inactive and display a faint fluorescence in the extreme red, at 685 nm, as a probable effect of an extended aggregation state. The corresponding fluorescence lifetime profiles in Figure S14 (Supporting Information) can be described by a double exponential law that returns two lifetimes of 1.4 and 2.9 ns (average lifetime $\tau^* = 1.8\,ns$) for CAR10 and 0.4 and 1.1 ns ($\tau^* = 0.7\,ns$) for RhB powders. The lifetime increase observed in CAR10 is indeed consistent with a higher emission efficiency. In Figure 7c, CA180 shows the characteristic blue emission of CA CDs. This emission is excitable at 360 nm and is compatible with the broad absorption band between 300 and 400 nm, as a result of radiative recombination from the C=O species. Less significant is the contribution of the higher-energy C=C structure. Considering the structural information provided by FTIR and NMR and the PL response, which is very similar to that of RhB dye, we can infer that the optical properties of CAR are not governed by quantum confinement effects. In other words, the physical-chemical characterization shown so far allows us to rule out any correlation with the size of the system and the presence of aromatic domains, which are characteristic of graphene quantum dots. CARs exhibit two distinct responses to light excitation. The first, characterized by high-energy, is a wavelength-dependent response, very similar to the CA system, and is characteristic of the disordered
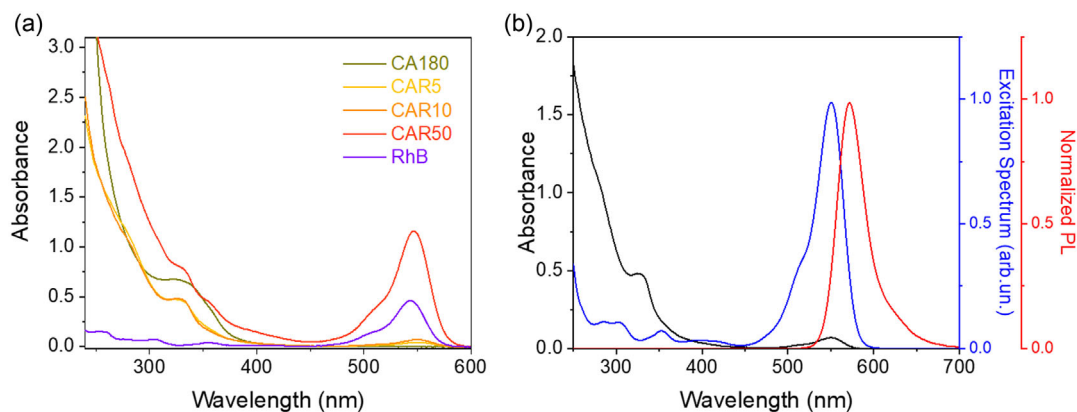

Figure 6. a) UV–vis absorption spectra of CA180, CAR5, CAR10, CAR50, and RhB ($1.5 \times 10^{-3}\,mg\,mL^{-1}$) in EtOH. b) UV–vis, excitation (monitored at 572 nm), and emission spectra of CAR10 (CDs concentration: $1.0 \times 10^{-2}\,mg\,mL^{-1}$).

**ADVANCED
SCIENCE NEWS**

www.advancedsciencenews.com

**small
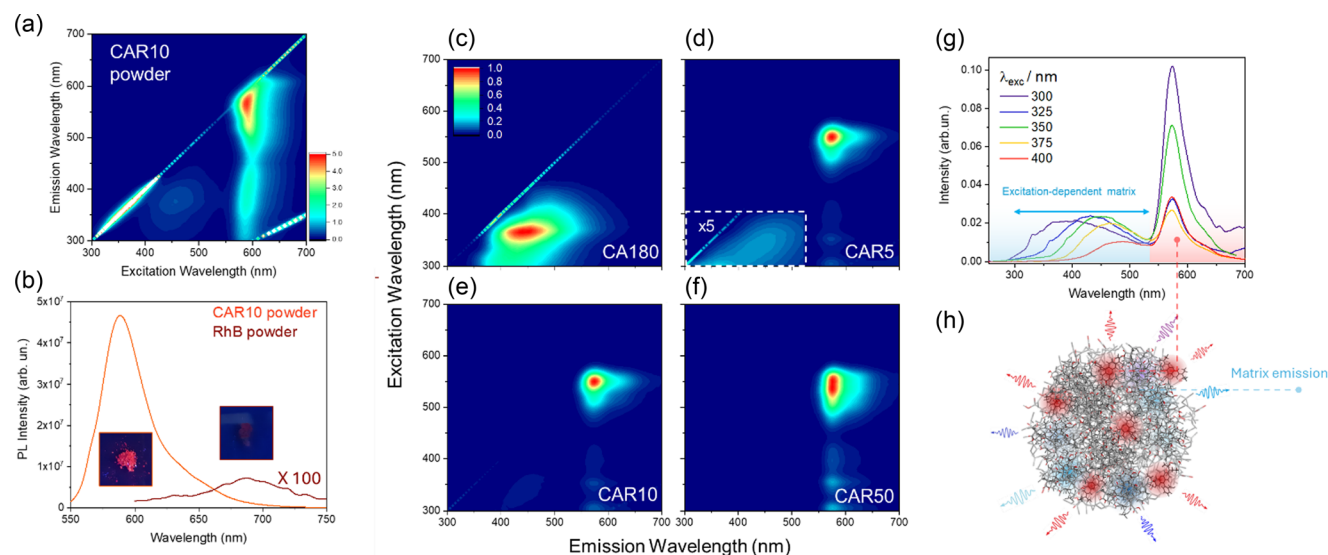structures**

www.small-structures.com

Figure 7. a) Excitation–emission spectra (x-axis, emission wavelength; y-axis, excitation wavelength; z-axis, intensity emission in false colors) of CAR10 powder. b) PL spectra of CAR10 and RhB powders with photographs under UV excitations. c–f) Excitation–emission maps of different CDs with the increase of RhB content. g) PL spectra of CAR10 at different excitation wavelengths: excitation-dependent contributions come from CA-derived carbon matrix. h) Drawing of a CAR dot: red centers are RhB dyes, and various blue tones account for matrix emission.

carbonaceous system. The second, which is the most intense, is related to the dye embedded in the framework and is independent of excitation as if it was diluted in a solvent (Figure 7g).

In summary, as displayed in Figure 7f, we can model the CARs behavior as a carbon matrix that does not perturb the optical properties of the dye since they operate like an inert dispersing medium. The shape of the map in the UV-blue region, however, appears to be slightly different from CA180 (undoped citric acid CDs). In particular, we observe a higher contribution at higher energy, indicating a probable influence of the RhB during the CDs formation process, as hypothesized in the FTIR and UV–vis analysis. At high dye concentrations (CAR50), RhB shows a broadening of the excitation range that we attribute to the formation of dimers in the CD structure.[44]

3.3. Solid-State Lasing

Silica monoliths were loaded with CARs to investigate solid-state laser emission properties. We designed organic–inorganic hybrid matrices from a sol composed of TEOS, TMSPMA, and the photo-initiator ethyl-2,4,6-trimethylbenzoylphenylphosphinate (TPB). The condensation reaction was catalyzed under acidic conditions using HCl. The silica monoliths, containing various types and concentrations of CARs, were cured with UV light at 365 nm for a few minutes, resulting in a solid, homogeneous, and transparent structure (**Figure 8**a). During UV curing, two processes occur simultaneously, although at different rates: polymerization of the organic component and inorganic polycondensation of the silica. The monolith's mechanical integrity is a balance between these processes, allowing flexible organic chains to form together with the stiff silica network. The hybrid nature of the matrix was optimized to minimize crack formation during gelification. The formation of the organic–inorganic structure, based on a sol

composition optimized in our previous study,[45] was monitored by using infrared spectroscopy.

The spectral features of the precursors are reported in Figure S15 (Supporting Information). Between 1070 and 1080 cm^{-1}, we observe the Si—O—CO asymmetrical stretching in silanols.[46] Si—O and C—O stretching are detectable between 718 and 882 cm^{-1}.[47] The C—H bending vibrations appear at 1160–1168 cm^{-1} and also populate the region around 1296 cm^{-1}.[48] At 1718 cm^{-1}, the TMSPMA shows a strong vibration corresponding to the C=O or methacrylate group.[49] FTIR was also used to monitor the photocuring process. Figure 8b illustrates the effects of UV exposure on the sol. During the first 120 s, there is a marked decrease in the intensity of the 1070 cm^{-1} mode, accompanied by an increase of the band near 1029 cm^{-1}. Over time, the spectral features between 1000 and 1035 cm^{-1} merge into a single, weakly modulated band with a peak at 1036 cm^{-1}, which is attributed to the hydrolysis of Si—$(OCH_2—CH_3)_4$ into $Si(OH)_4$ and the subsequent condensation into Si—O—Si groups.[50]

For the organic component, an increase in the band at 1698 cm^{-1} is observed during the first 120 s of UV irradiation. This is associated with the polymerization process, where the C=O group vibrational intensity is modulated by the conversion of the methacrylate double bond (C=C) into a single bond (C—C), resulting in the creation of polymer links. As polymerization and condensation progress, the vibrational intensity in this region also diminishes.[51] This study was carried out on an ATR platform under low-intensity exposure to examine the matrix solidification process. Figure S15b (Supporting Information) compares the infrared spectrum of a typical monolith after UV-curing with the spectrum of a monolith subjected to a subsequent thermal treatment at 300 °C for 1 h. The comparison reveals a strong presence of Si—O—Si linkages in the inorganic component and the splitting of the C=O band at around 1700 cm^{-1}. Although the polycondensation regime in the
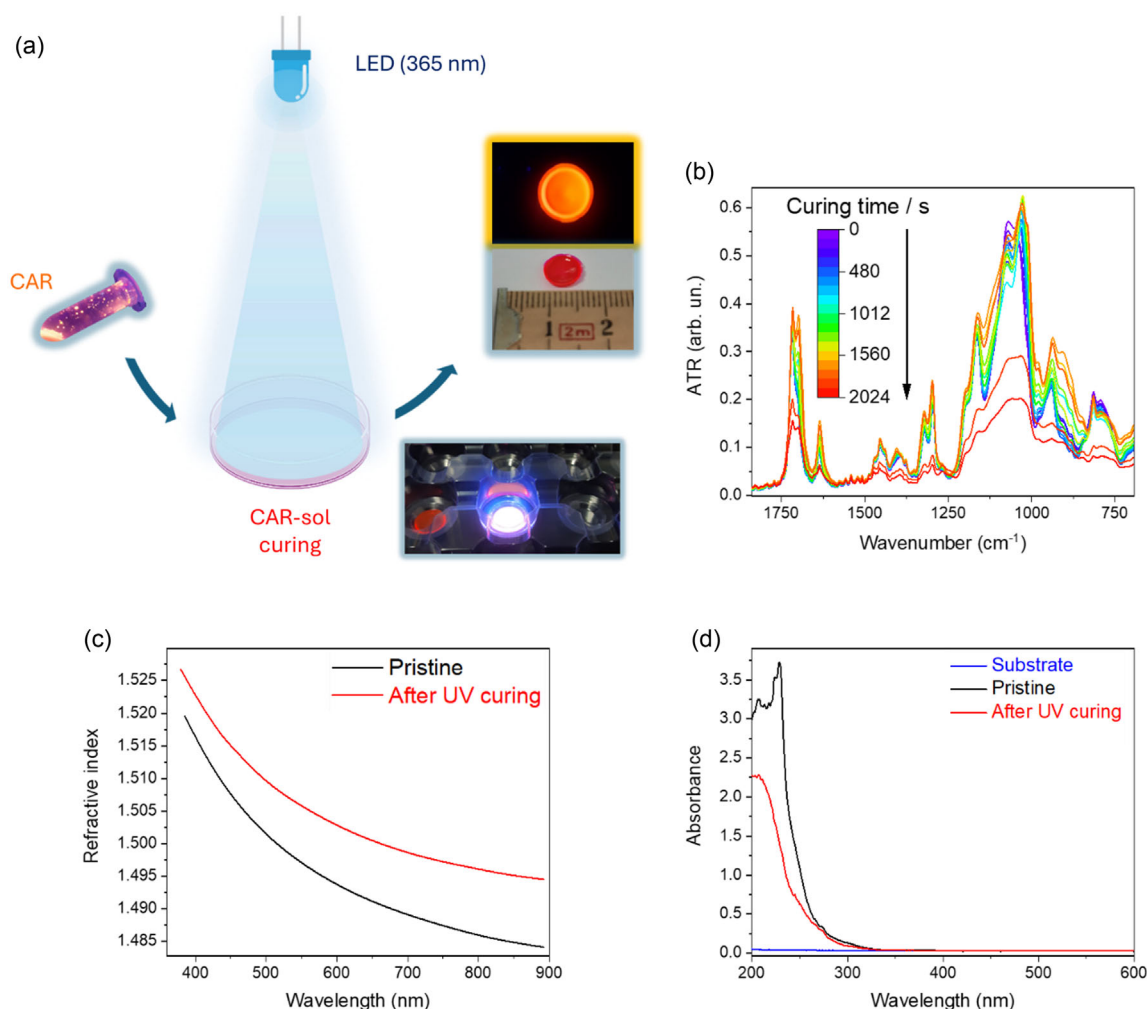
Figure 8. a) Scheme of monolith fabrication and examples of small luminescent CAR-based silica monolith. b) ATR study of polymerization and condensation process of 10 µL of sol. c) Refractive index of deposited films before and after UV curing. d) UV–vis of hybrid silica films.

UV-cured sample is not as pronounced as in the thermally treated sample, it still provides substantial structural support to the monolith in conjunction with the organic part. The organic component is significantly reduced in the 300 °C treated sample, resulting in increased fragility. Additionally, we examined the photopolymerized film after one week of aging (Figure S15c, Supporting Information). The aging process does not affect the organic counterpart in the monolith but promotes the silica condensation, as proved by the rise of the 1100 cm^{-1} band.

Spectroscopic ellipsometry allowed for estimating the refractive index and thickness of hybrid films before and after UV curing (Figure 8c). The refractive index as a function of wavelength was modeled by using the Cauchy dispersion equation: $n(k) = A_n + B_n/k^2 + C_n/k^4$. Here, A_n represents a parameter associated with the material average refractive index, while B_n and C_n modulate the n trend as a function of the wavelength. The deposited film (pristine) shows a thickness of around 670 nm, without significant variation after curing. After UV exposure, the refractive index at 632.8 nm increases from 1.49 to 1.50 as the effect of successful condensation and polymerization.[45]

The film deposited on the silica substrate was also investigated by UV–vis absorption (Figure 8d). The pristine film displays strong absorption below 250 nm, attributed to the presence of unreacted silanes and TBP photoinitiator. During UV curing, the absorption band diminishes, reflecting the formation of Si—O—Si groups, the photoinduced homolytic cleavage of the photoinitiator, and the resulting polymerization of the methacrylate groups of TMSPMA. After photocuring, the film exhibits high transparency in the near UV and visible range, only slightly influenced by thickness. A monolith with a thickness of 2.5 mm (Figure S16, Supporting Information) only shows a weak absorption band extending up to 400 nm. Overall, the hybrid silica monolith serves as an excellent host for testing the optical properties of CARs.

To explore the potential applications as a laser medium, we investigated the fluorescence quantum yield (PLQY), fluorescence lifetime (t_r), and radiation transition rate (K_r), of two nanocomposite systems, named CAR10@SiO$_2$ and RhB@SiO$_2$, obtained by embedding CAR10 and RhB into the hybrid silica matrix. The PLQYs of RhB@SiO$_2$ and CAR10@SiO$_2$ are

relatively high, 58% and 48%, respectively, more than sufficient to achieve lasing operation. Figure S17 (Supporting Information) shows the two normalized emission decay profiles that can be fitted by a single exponential decay model. The t_r values of CAR10@SiO$_2$ and RhB@SiO$_2$ are estimated to be ≈5.32 and 6.19 ns, respectively, and the corresponding radiation transition rates, defined as $k_r = QY/t_r$, are ≈9.02 and 9.36 × 10^7 sec^{-1}. No significant changes are observed between the molecular RhB and CAR10, indicating that the dye incorporation inside the carbonaceous matrix does not significantly affect the optical response.

3.4. Random Lasing Experiment on CAR in the Silica Matrix

Circular silica hybrid monoliths with a diameter of 5 mm and a thickness of 1 mm (Figure 8a) were loaded with the same amount (in mass) of CAR 5, CAR10, and CAR50. The samples were excited along a strip produced by focusing the excitation beam through a cylindrical lens, and the emission was collected by an optical fiber at ≈90° with respect to pump beam. The results are summarized in **Figure 9**. At high pumping power, all samples exhibit a narrowing of the emission, together with a nonlinear response with respect to energy of the pump beam (E_{in}). These phenomena clearly indicate the onset of light amplification by stimulated emission. The achievement of laser gain in a disordered system without the need for mirrors or any external cavity is often described in the literature as random lasing.[25,52,53] Indeed, light amplification phenomena in Figure 9 are likely favored by the disordered nature of the CAR host

matrix, giving rise to light scattering events that increase the optical path, while photoexcited RhB is well known for its high gain coefficient.[54]

The samples CAR5 and CAR10, which have the lowest RhB doping levels, display similar spectral characteristics below excitation fluences of ≈0.84 and 0.67 mJ pulse^{-1}, respectively. Beyond these thresholds, a narrowing of the full width at half maximum (FWHM) is observed, particularly for CAR10, which narrows to about 9 nm. CAR50, however, shows the lowest threshold at 0.12 mJ pulse^{-1}, with the FWHM stabilizing at 9 nm, achieved at around 0.1 mJ pulse^{-1}. The laser threshold of 0.12 mJ pulse^{-1} displayed by CAR50 (Figure 9f) corresponds to a local beam fluence of 11 mJ cm^{-2}. If we also take into account the pulse duration of 5 ns, we can estimate that the laser threshold is reached at a pumping intensity of 2.3 MW cm^{-2}.

In CAR5 and CAR10, the maximum spontaneous emission is observed at ≈598 nm, which blueshifts by 4 nm in the amplification regime. For CAR50, the spectral maximum of the emission above amplification threshold occurs at 598 nm, with a redshift of 3 nm compared to low-power conditions.

Interestingly, the gain curves observed in Figure 9 are highly dependent on the concentration of RhB, a phenomenon likely ascribable to the carbonaceous matrix, which prevents dye quenching by maintaining a localized concentration of active optical centers. This, in turn, influences the main free path of radiation within the random structure, a critical factor for establishing random laser emission. Improvement in random lasing characteristics of CARs with RhB loading is observed (Figure 9b,c) not only because of the expected increase of the
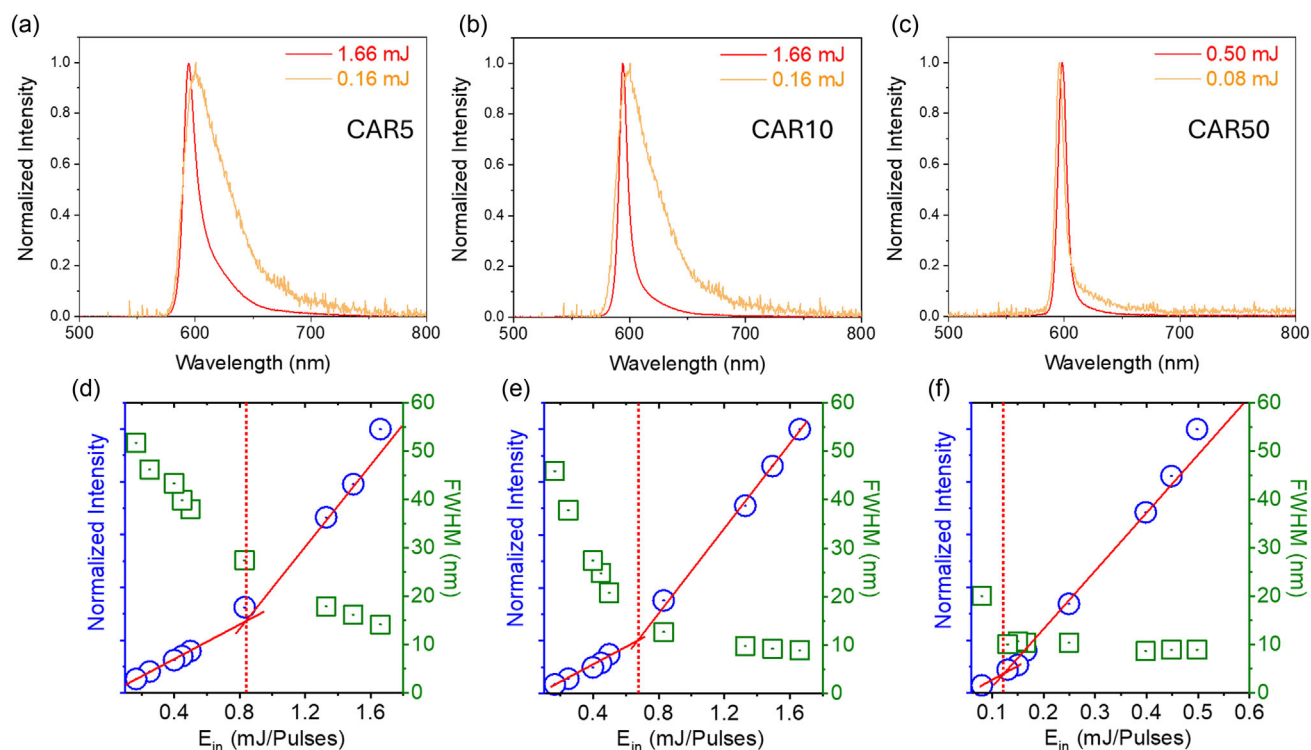

Figure 9. Emission response of CAR10 under pulsed laser at 540 nm. a–c) Spectral emission of CAR5, CAR10, and CAR50 below and above the amplification threshold. d–f) Output characteristics as a function of pumping power (mJ/pulse).

gain, but also because of the possibility of multiple scattering of photons by the increasing number of carbonaceous centers, in addition to the imperfections in silica matrix.

The impact of the sintering process on the CARs properties was investigated by treating CAR10 at temperatures of 200 and 220 °C. The results are shown in Figure S18 (Supporting Information). The postsynthetic heat treatment affects the optical properties of CAR10. Annealing at 200 °C does not influence the spectral characteristics of CARs below and above the lasing threshold, although we observed an increase in the threshold after treatment. This effect is more evident at 220 °C, where we observed a broadening of spectral emission toward higher wavelengths. In this case, the threshold rises above 0.9 mJ pulse^{-1}. We ascribed this effect to the deterioration of RhB when exceeds its melting temperature (199 °C).[27] The higher sintering temperature (240 °C), in contrast, results in the complete loss of lasing capability at the investigated power regime (Figure S18d, Supporting Information).
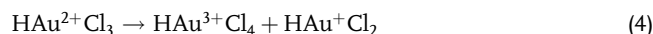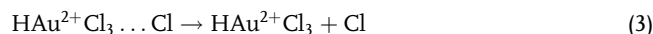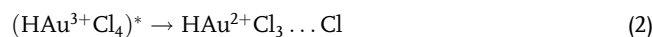
3.5. Effect of TiO$_2$ NPs as Scattering Centers

The optical properties were further examined after incorporating scattering centers into the monoliths to favor the random lasing phenomenon. Commercial TiO$_2$ (P25) NPs, with a nominal size of 21 nm, were added to the sol before photocuring. We investigated the effect of scattering center concentration on CAR10, the CDs with intermediate RhB concentration, by testing two concentrations of TiO$_2$ quantified as mg added per sol volume: 0.37 mg mL^{-1} (CAR10TO1) and 3.70 mg mL^{-1} (CAR10TO10). The resulting lasing response is reported in Figure S19 (Supporting Information). Concerning CAR10, CAR10TO10 exhibits a lower lasing threshold (0.43 mJ pulse^{-1}) and reduces the FWHM to about 7 nm, indicating that the scattering produced by TiO$_2$ enhances the random laser action of CAR10. Increasing the TiO$_2$ concentration, adversely affects the lasing of CAR10, raising the threshold to 0.82 mJ pulse^{-1}, and preventing the FWHM from dropping below 10 nm. This reduced efficiency at higher concentrations suggests that various effects, such as quenching of CARs due to contact with TiO$_2$, influence the optical properties of the monolith.

The addition of TiO$_2$ appears to improve the lasing performance of both CAR5 and CAR10, which have lower RhB concentrations and are more diluted in the carbon matrix, making them less prone to interact with TiO$_2$. Conversely, while TiO$_2$ does not significantly affect the lasing threshold, it does cause a redshift of the maximum toward 604 nm in CAR50 (Figure S20, Supporting Information).

3.6. Effect of Au NPs as Scattering Centers

The photopolymerization process of the hybrid organic–inorganic matrix can be exploited for the in situ nucleation and growth of scattering centers. Indeed, we modified the nanocomposite structure by dissolving increasing concentrations of HAuCl$_4$, as a gold NPs precursor, in the hybrid silica sol. Under UV exposure, HAuCl$_4$ is subject to photoreduction[55] according to the reaction steps:

$$HAu^{3+}Cl_4 \xrightarrow{h\nu} (HAu^{3+}Cl_4)^* \tag{1}$$

$$(HAu^{3+}Cl_4)^* \rightarrow HAu^{2+}Cl_3 \ldots Cl \tag{2}$$

$$HAu^{2+}Cl_3 \ldots Cl \rightarrow HAu^{2+}Cl_3 + Cl \tag{3}$$

$$HAu^{2+}Cl_3 \rightarrow HAu^{3+}Cl_4 + HAu^+Cl_2 \tag{4}$$

$$HAu^+Cl_2 \xrightarrow{h\nu} Au^0 + HCl + Cl \tag{5}$$

$$nAu^0 \rightarrow (Au^0)_n \tag{6}$$

The reaction was monitored via UV–vis absorption in the sol without CDs (**Figure 10**a). The progressive reduction of HAuCl$_4$ is evidenced by the decrease in the band at 322 nm (Figure S21, Supporting Information) and the corresponding emergence of the plasmonic band at 545 nm. Figure 10b shows the XRD pattern of the silica monolith with in situ growth of Au NPs, characterized by the prominent amorphous band of silica at 20°. At $2\theta = 38.2°$ and 44.4°, the (111) and (200) Bragg reflections of the face-centered (FCC) lattice are observed.[56] The crystal structure of the Au NPs was further examined using TEM, as shown in Figure 10c. The nanocomposites were at first ground to obtain a fine powder, suspended in ethanol, and then drop-casted at room temperature onto a SiO$_2$ grid. The size distribution histogram, calculated for 730 Au NPs from multiple HAADF-STEM images at various magnifications, is shown in Figure 10d. The images at high resolution were analyzed by calculating the two-dimensional FT to determine the lattice parameters and crystal symmetry of individual NPs, with the zero-order beam (ZB) marked by a white circle (Figure 10e,f). The average fringe distance of $d = 2.1 \pm 0.1$ Å corresponds to lattice-plane distances $(0\,2\,0) = 2.0395$ Å in FCC Au. Figure 10e reports HRTEM image of a single Au NP, whose crystalline pattern is in accordance with an FCC structure as indicated by its 2-dimensional FT. The calculated diffraction pattern is typical of a slightly distorted structure (space group Fm-3m, space group number 225)[57] with a lattice parameter of $a = 4.07894$ Å in the [101]-zone axis.

EDXS elemental maps of in situ-grown Au NPs within the silica monolith were performed to study in detail the interaction at the metal/dielectric interface (Figure S22, Supporting Information). Furthermore, focusing on a single NP, we investigated the structure and the interaction with the chemical environment after the growth process (**Figure 11**a). EDXS elemental maps of Si, Au, and O, along with the overlapping Au and Si EDXS maps, suggest the formation of Au crystalline core surrounded by a denser hybrid silica shell. Concerning the quantification of the EDXS line spectra measured from complex NPs, one must consider that only compositions averaged along the electron-beam direction, i.e., the whole volume along the electron trajectory contributes to the detected X-ray signal. However, the composition of different regions of a core-shell NP can be determined by applying the subshell approach.[58,59] The Au- and Si-distributions within single NPs after the SiO$_2$ substrate correction can be used to determine the composition of the core and shell of the particles. The analysis reveals that the thin denser hybrid silica shell is ≈1 nm thick (Figure 11b,c). This suggests that during the polymerization process, the local increase in pH, produced by the gold reduction, promotes a
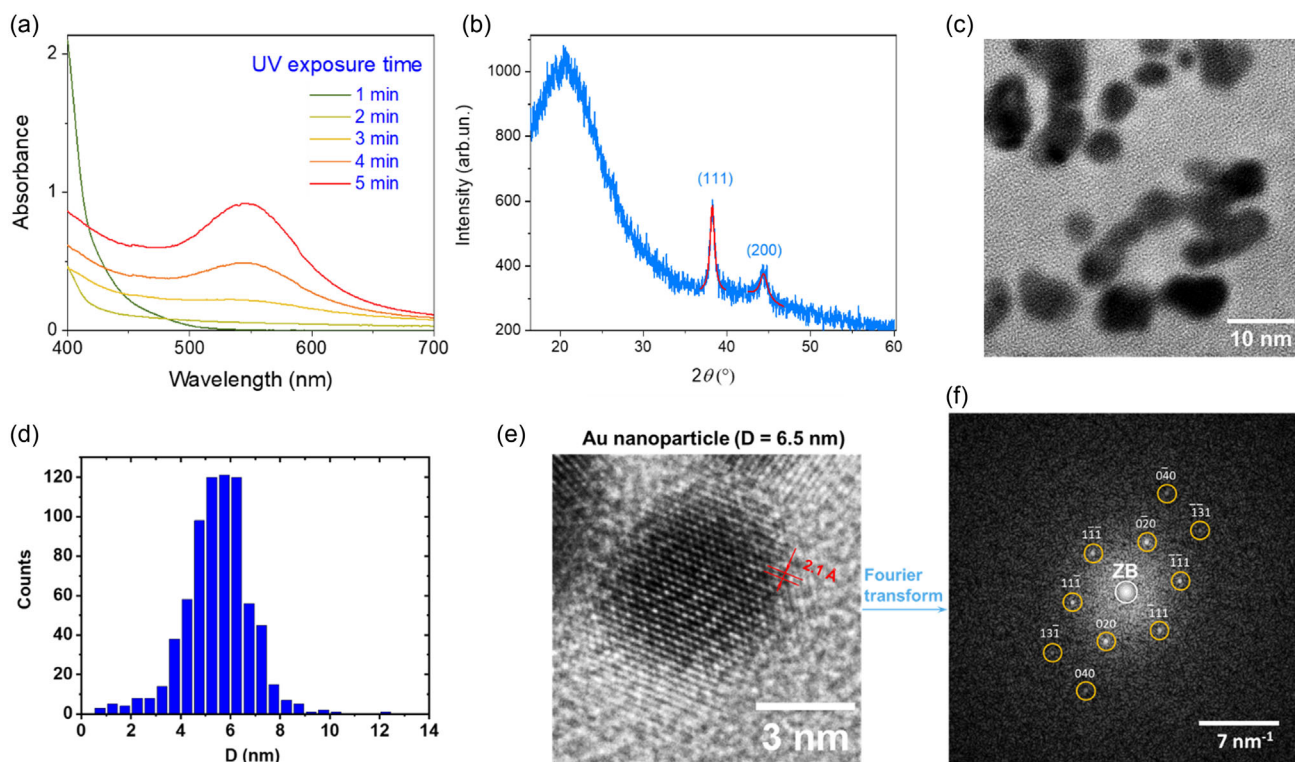
ADVANCED
SCIENCE NEWS

www.advancedsciencenews.com

small
structures

www.small-structures.com

Figure 10. a) Plasmonic resonance detected by UV–vis in $HAuCl_4$ + sol solution under UV irradiation in the first 5 min of curing process ($HAuCl_4$ concentration: 1.06 mg mL^{-1}). b) XRD pattern of the cured $HAuCl_4$ + sol solution. Au peaks are highlighted by two Lorentzian curves. c) Typical TEM images of Au NPs in silica matrix. d) Au NPs size distribution calculated by TEM images. e) HRTEM image of a single Au NPs and f) relative Fourier transform (FT).
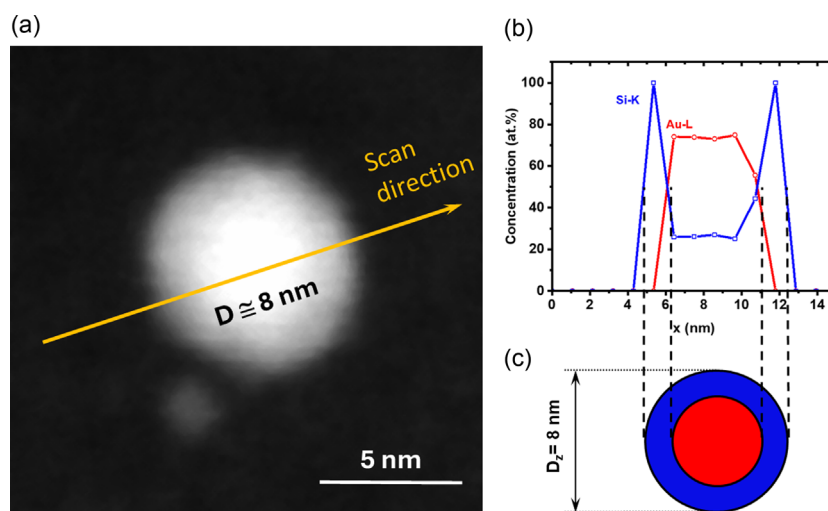
Figure 11. a) HAADF-STEM image of a single Au-Si core-shell NP in CAR10. The orange arrow indicates the EDXS line scan. b) Normalized Au- and Si-concentration profiles along the line scan. c) Schematic of the denser hybrid silica matrix surrounding the gold NP.

larger polycondensation of the silanols groups, leading to a denser structure around the Au NPs.

Considering the optical properties of the monoliths, Au NPs offer both threshold and spectral advantages. As shown in **Figure 12**, random lasing in the presence of in situ-grown gold

particles was tested on CAR10. We find that the addition of Au reduces the lasing threshold below 0.40 mJ pulse^{-1}. The lowest threshold was achieved at a concentration of 1.06 mg mL^{-1} of Au precursor in the sol (CAR10Au1.06), with an FWHM as low as 5 nm, rarely matched by other literature reports of amplified
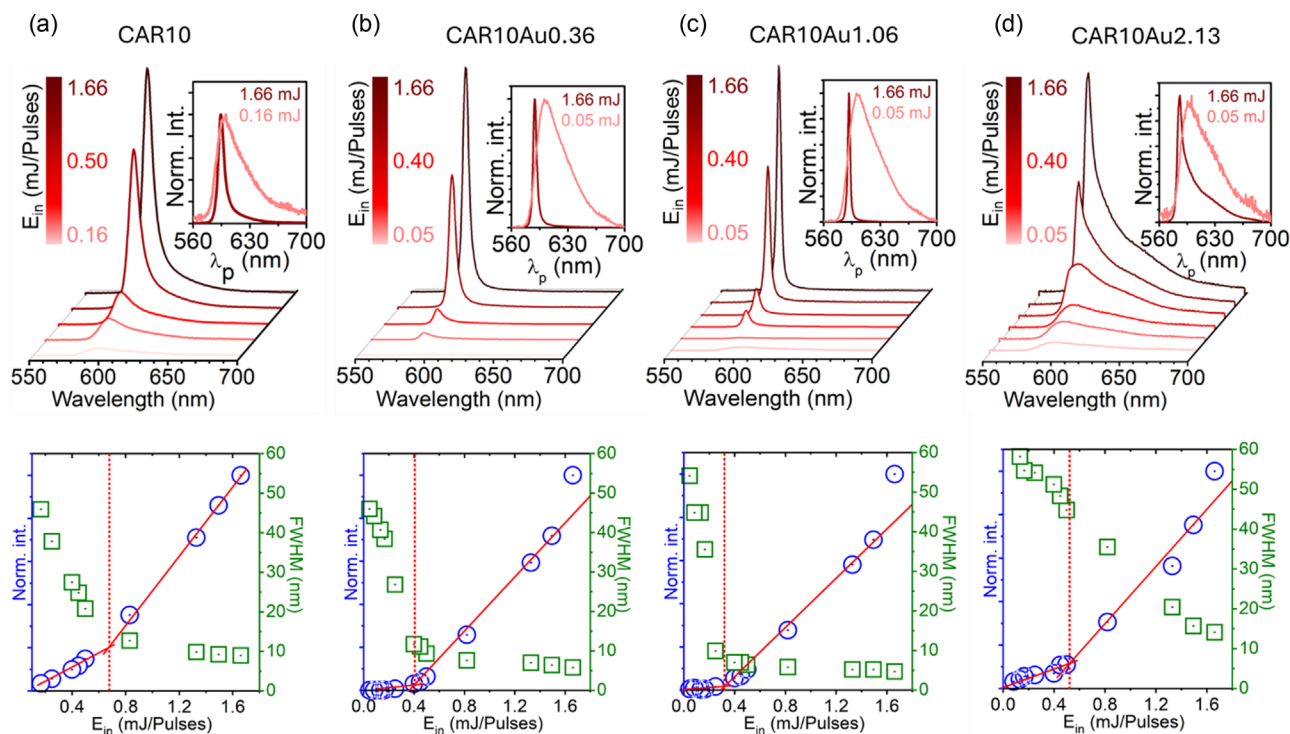
ADVANCED
SCIENCE NEWS
www.advancedsciencenews.com

small
structures
www.small-structures.com

Figure 12. Effect of Au nanoscatterers on CAR10 emission in silica matrix as a function of the $HAuCl_4$ concentration in the sol: a) no $HAuCl_4$ (reference), b) 0.36, c) 1.06, and d) 2.13 mg mL^{-1}. Top: spectral emission under 0.05 mJ (below threshold) and 1.66 mJ (above threshold) powers under excitation at 540 nm. Bottom: output characteristics as a function of pumping power (mJ/pulse).

stimulated emission or random lasing of CD-based systems. We observe that the lasing peak is slightly shifted to shorter wavelengths compared to the fluorescence maximum, likely because the wavelength dependence of the gain profile differs from that of the fluorescence cross-section. Likewise TiO_2, too high a concentrations of gold particles might cause the deterioration of random lasing performance. The interpretation of this mechanism is complex and deserves a dedicated study. One effect of in situ growth of gold NPs is the formation of a denser hybrid silica shell, suggesting a mechanism similar to that observed for TiO_2. Here, the increased $HAuCl_4$ concentration in the sol leads to an increase in NPs concentration likely fostering a photoelectron transfer mechanism and leading to CAR quenching. This implies that while in situ growth is a very effective method for creating a scattering medium for random lasing applications with remarkably good performance, a careful optimization of the architecture of the composites is still needed to avoid performance degradation, like the more common random systems.

4. Conclusion

We synthesized CDs by taking advantage of the CA thermal degradation, which facilitates the formation of weakly fluorescent CDs. The matrices successfully incorporate dye molecules without affecting their emission properties, allowing their use in solid-state applications. The RhB-loaded CDs serve as a gain medium for developing silica-based materials functioning as random lasing systems. Random lasing regime can be easily achieved by exploiting the inherent scattering properties of the carbonaceous dots, as well as imperfections of the host silica matrix, however, the random lasing performance can be controlled and substantially enhanced by appropriately introducing scattering media during the photopolymerization of the hybrid silica host. The flexibility provided by the materials synthesis allows introducing an innovative one-step strategy to create a medium for random lasing applications. During the photocuring of the hybrid organic–inorganic network, the UV exposure triggers the nucleation and growth of gold nanoscatterers, featuring controlled size distribution and plasmonic properties. The resulting nanocomposite monoliths lase in the region between 580 and 610 nm exhibiting a lasing threshold and a FWHM that are dependent on the CDs loading and scattering centers concentration. Overall, the optical response of the nanocomposites is compatible with an incoherent random lasing regime, characterized by a low lasing threshold and a spectral emission width of less than 5 nm.

The present approach, which combines matrix solution processing and targeted design of carbon-based NPs, emerged as an ideal method for producing a wide variety of solid-state disordered active media to be tested as random lasing systems.

Supporting Information

Supporting Information is available from the Wiley Online Library or from the author.

Conflict of Interest

The authors declare no conflict of interest.

Author Contributions

Luigi Stagi: conceptualization (lead); formal analysis (lead); investigation (lead); methodology (lead); writing—original draft (lead); writing—review & editing (lead). **Davide Carboni**: formal analysis (lead). **Roberto Anedda**: formal analysis (equal); investigation (equal). **Radian Popescu**: formal analysis (equal); investigation (lead). **Yolita Eggeler**: formal analysis (equal). **Laura Calvillo**: data curation (lead); formal analysis (lead); investigation (lead). **Ashim Pramanik**: formal analysis (lead); investigation (lead). **Alice Sciortino**: formal analysis (lead); investigation (lead). **Marco Cannas**: formal analysis (supporting). **Fabrizio Messina**: conceptualization (lead); formal analysis (lead); validation (lead); writing—review & editing (lead). **Luca Malfatti**: conceptualization (lead); funding acquisition (lead); supervision (lead); validation (lead); writing—original draft (lead); writing—review & editing (lead).

Data Availability Statement

The data that support the findings of this study are available from the corresponding author upon reasonable request.

[1] H. Lin, J. Huang, L. Ding, *J. Nanomater.* **2019**, *2019*, https://doi.org/10.1155/2019/5037243.

[2] S. Chahal, N. Yousefi, N. Tufenkji, *ACS Sustain. Chem. Eng.* **2020**, *8*, 5566.

[3] Y. Park, Y. Kim, H. Chang, S. Won, H. Kim, W. Kwon, *J. Mater. Chem. B* **2020**, *8*, 8935.

[4] J. Zhang, X. Lu, D. Tang, S. Wu, X. Hou, J. Liu, P. Wu, *ACS Appl. Mater. Interfaces* **2018**, *10*, 40808.

[5] L. Malfatti, M. Poddighe, L. Stagi, D. Carboni, R. Anedda, M. F. Casula, B. Poddesu, D. De Forni, F. Lori, S. Livraghi, A. Zollo, L. Calvillo, P. Innocenzi, *Adv. Funct. Mater.* **2024**, *34*, 2404511.

[6] S. Y. Song, K. K. Liu, Q. Cao, X. Mao, W. B. Zhao, Y. Wang, Y. C. Liang, J. H. Zang, Q. Lou, L. Dong, C. X. Shan, *Light Sci. Appl.* **2022**, *11*, 1.

[7] B. Wang, Z. Wei, L. Sui, J. Yu, B. Zhang, X. Wang, S. Feng, H. Song, X. Yong, Y. Tian, B. Yang, S. Lu, *Light Sci. Appl.* **2022**, *11*, https://doi.org/10.1038/s41377-022-00865-x.

[8] H. Ding, X.-X. Zhou, J.-S. Wei, X.-B. Li, B.-T. Qin, X.-B. Chen, H.-M. Xiong, *Carbon* **2020**, *167*, 322.

[9] Y. Zhang, S. Ding, J. Yu, L. Sui, H. Song, Y. Hu, G. I. N. Waterhouse, Z. Tang, S. Lu, *Matter* **2024**, *7*, 3518.

[10] D. Ni, M. Späth, F. Klämpfl, M. Hohmann, *Sensors* **2023**, *23*, 1.

[11] B. D. Mansuriya, Z. Altintas, *Nanomaterials* **2021**, *11*, 1.

[12] S. Yang, W. Li, C. Ye, G. Wang, H. Tian, C. Zhu, P. He, G. Ding, X. Xie, Y. Liu, Y. Lifshitz, S. T. Lee, Z. Kang, M. Jiang, *Adv. Mater.* **2017**, *29*, https://doi.org/10.1002/adma.201605625.

[13] F. Yuan, T. Yuan, L. Sui, Z. Wang, Z. Xi, Y. Li, X. Li, L. Fan, Z. Tan, A. Chen, M. Jin, S. Yang, *Nat. Commun.* **2018**, *9*, 1.

[14] K. Bramhaiah, R. Bhuyan, S. Mandal, S. Kar, R. Prabhu, N. S. John, M. Gramlich, A. S. Urban, S. Bhattacharyya, *J. Phys. Chem. C* **2021**, *125*, 4299.

[15] R. Ludmerczki, L. Malfatti, L. Stagi, M. Meloni, C. M. Carbonaro, M. F. Casula, D. Bogdan, S. Mura, I. M. Mandity, P. Innocenzi, *Chem. - A Eur. J.* **2021**, *27*, 2543.

[16] B. Bartolomei, M. Prato, *Small* **2023**, *19*, 1.

[17] J. Ren, L. Malfatti, P. Innocenzi, *C* **2020**, *7*, 2.

[18] F. Arcudi, L. Đorđević, *Small* **2023**, *19*, https://doi.org/10.1002/smll.202300906.

[19] J. Ren, L. Stagi, P. Innocenzi, *Prog. Solid State Chem.* **2021**, *62*, 100295.

[20] B. Zhao, H. Ma, M. Zheng, K. Xu, C. Zou, S. Qu, Z. Tan, *Carbon Energy* **2022**, *4*, 88.

[21] B. Wang, G. I. N. Waterhouse, B. Yang, S. Lu, *Acc. Chem. Res.* **2024**, *57*, 2928.

[22] M. Meloni, L. Stagi, D. Sanna, S. Garroni, L. Calvillo, A. Terracina, M. Cannas, F. Messina, C. M. Carbonaro, P. Innocenzi, L. Malfatti, *Nanomaterials* **2022**, *12*, 2351.

[23] A. S. L. Gomes, D. Valente, H. P. de Oliveira, S. J. L. Ribeiro, C. B. de Araújo, *Opt. Mater. X* **2022**, *16*, 100203.

[24] Y. Zhang, S. Lu, *Chem* **2024**, *10*, 134.

[25] A. Pramanik, M. Reale, M. Cannas, R. Popescu, A. Sciortino, F. Messina, *ACS Photonics* **2024**, *11*, 3035.

[26] R. Gayathri, C. S. Suchand Sandeep, C. Vijayan, V. M. Murukeshan, *Nanomaterials* **2023**, *13*, 2466.

[27] S. Qiu, H. Chu, Y. Zou, C. Xiang, H. Zhang, L. Sun, F. Xu, *J. Therm. Anal. Calorim.* **2016**, *123*, 1611.

[28] M. Barbooti, D. Al-Sammerrai, *Thermochim. Acta* **1986**, *98*, 119.

[29] D. Wyrzykowski, E. Hebanowska, G. Nowak-Wiczk, M. Makowski, L. Chmurzyński, *J. Therm. Anal. Calorim.* **2011**, *104*, 731.

[30] A. A. Sapalidis, *Symmetry* **2020**, *12*, 1.

[31] S. H. S. Boddu, P. Bhagav, P. K. Karla, S. Jacob, M. D. Adatiya, T. M. Dhameliya, K. M. Ranch, A. K. Tiwari, *J. Funct. Biomater.* **2021**, *12*, 58.

[32] S. Matsumura, A. R. Hlil, C. Lepiller, J. Gaudet, D. Guay, Z. Shi, S. Holdcroft, A. S. Hay, *J. Polym. Sci., Part A: Polym. Chem.* **2008**, *46*, 7207.

[33] W. Kwon, Y. H. Kim, C. L. Lee, M. Lee, H. C. Choi, T. W. Lee, S. W. Rhee, *Nano Lett.* **2014**, *14*, 1306.

[34] P. Pimpang, R. Sumang, S. Choopun, *Chiang Mai J. Sci.* **2018**, *45*, 2005.

[35] L. J. Bellamy, *The Infra-Red Spectra of Complex Molecules*, Springer Dordrecht, Dordrecht **1975**.

**ADVANCED
SCIENCE NEWS**

www.advancedsciencenews.com

**small
structures**

www.small-structures.com

[36] A. Pourjavadi, Z. Mazaheri Tehrani, R. Heydarpour, Z. Masihzadeh, *Sens. Imaging* **2023**, *24*, 37.

[37] L. D'Souza, P. Devi, M. P. Divya Shridhar, C. G. Naik, *Anal. Chem. Insights* **2008**, *2008*, 135.

[38] M. C. Galanti, A. V. Galanti, *J. Org. Chem.* **1982**, *47*, 1572.

[39] A. V. Galanti, B. T. Keen, R. H. Pater, D. A. Scola, *J. Polym. Sci. Polym. Chem. Ed.* **1981**, *19*, 2243.

[40] G. D. Cody, N. Z. Boctor, R. M. Hazen, J. A. Brandes, H. J. Morowitz, H. S. Yoder, *Geochim. Cosmochim. Acta* **2001**, *65*, 3557.

[41] A. B. Siddique, A. K. Pramanick, S. Chatterjee, M. Ray, *Sci. Rep.* **2018**, *8*, 1.

[42] K. J. Mintz, M. Bartoli, M. Rovere, Y. Zhou, S. D. Hettiarachchi, S. Paudyal, J. Chen, J. B. Domena, P. Y. Liyanage, R. Sampson, D. Khadka, R. R. Pandey, S. Huang, C. C. Chusuei, A. Tagliaferro, R. M. Leblanc, *Carbon* **2021**, *173*, 433.

[43] S. Wang, Z. G. Chen, I. Cole, Q. Li, *Carbon* **2015**, *82*, 304.

[44] Q. Yuan, X. Zhang, Z. Wang, M. H. M. A. Shibraen, S. Yang, J. Xu, *Colloids Surf., A* **2015**, *486*, 139.

[45] S. Costacurta, L. Malfatti, P. Falcaro, P. Innocenzi, *J. Sol-Gel Sci. Technol.* **2007**, *44*, 59.

[46] F. Rubio, J. Rubio, J. L. Oteo, *Spectrosc. Lett.* **1998**, *31*, 199.

[47] N. Primeau, C. Vautey, M. Langlet, *Thin Solid Films* **1997**, *310*, 47.

[48] M. C. Matos, L. M. Ilharco, R. M. Almeida, *J. Non. Cryst. Solids* **1992**, *147–148*, 232.

[49] L. B. Canto, L. A. Pessan, *Polym. Test.* **2002**, *21*, 35.

[50] A. Wajda, W. H. Goldmann, R. Detsch, A. R. Boccaccini, M. Sitarz, *J. Non. Cryst. Solids* **2019**, *511*, 86.

[51] K. Liu, P. Gu, K. Hamaker, Z. H. Fan, *J. Colloid Interface Sci.* **2012**, *365*, 289.

[52] D. S. Wiersma, *Nat. Phys.* **2008**, *4*, 359.

[53] Y. Zhang, J. Wang, L. Wang, R. Fu, H. Sui, H. Song, Y. Hu, S. Lu, *Adv. Mater.* **2023**, *35*, 1.

[54] A. Machnev, D. Ofer, I. Shishkin, V. Kozlov, C. Diaferia, A. Accardo, G. Morelli, B. Apter, A. Inberg, G. Rosenman, P. Ginzburg, *Sci. Rep.* **2021**, *11*, 1.

[55] K. Kurihara, J. H. Fendler, J. Kizling, P. Stenius, *J. Am. Chem. Soc.* **1983**, *105*, 2574.

[56] S. Krishnamurthy, A. Esterle, N. C. Sharma, S. V. Sahi, *Nanoscale Res. Lett.* **2014**, *9*, 1.

[57] M. E. Straumanis, *Monatsh. Chem./Chem. Mon.* **1971**, *102*, 1377.

[58] C. Kind, R. Popescu, R. Schneider, E. Müller, D. Gerthsen, C. Feldmann, *RSC Adv.* **2012**, *2*, 9473.

[59] D. Hudry, I. A. Howard, R. Popescu, D. Gerthsen, B. S. Richards, *Adv. Mater.* **2019**, *31*, 1900623.